Multicomponent ambient noise cross-correlation at Forties

Jason P. Chang

ABSTRACT

Using the passive portion of the continuous recordings from the Apache Forties data set, I characterize the marine ambient noise field and perform ambient noise cross-correlations on multicomponent ocean-bottom node data. Spectrograms from nodes near and far from the operating platform suggest that the platform dominates the ambient noise field for frequencies up to 40 Hz, particularly in the vertical geophones. Plots of spectral power at each node as a function of distance from the operating platform support this observation. Beamforming of the ambient noise field across different subsections of the array confirms this widespread influence of the platform. As Love waves often have higher signal-to-noise ratio than corresponding Rayleigh waves, I apply the ambient noise cross-correlation method to multicomponent ocean-bottom node recordings. In the microseism band, I am able to recover coherent Scholte waves in the radial-radial correlations and coherent Love waves in the transverse-transverse correlations. For frequencies between 5 and 10 Hz, Love-wave energy appears to be just as coherent as Scholte-wave energy. Additionally, there are signs of an acoustic wave traveling on the hydrophone and vertical geophone components at very high frequencies ($40-80$ Hz). The presence of these acoustic waves is potentially promising for future work in passive fathometry.

INTRODUCTION

A number of studies have shown that an estimate of the interface-wave portion of the Green's function between two receivers can be obtained by cross-correlating simultaneous recordings of ambient seismic noise at those receivers (Lobkis and Weaver, 2001; Snieder, 2004; Wapenaar, 2004). The resulting travel times of these waves are then often used to tomographically image the Earth's subsurface. While most of the successful applications of this technique have occurred at the regional and continental scales (e.g., Shapiro et al., 2005; Yang et al., 2008; Bensen et al., 2008), there have been more recent breakthroughs at the local scale. In the land environment, Lin et al. (2012) used energy in the microseism band (between 0.1 and 2.0 Hz) to image the subsurface down to hundreds of meters, while Chang et al. (2016) used traffic energy around 3 Hz to image the subsurface down to tens of meters at Long Beach, California. In the marine environment, de Ridder and Dellinger (2011) and Mordret et al. (2013) processed ocean-bottom cable recordings of ambient noise to

recover inter-station Scholte waves in the microseism band at the Valhall oil field, which were then used to tomographically image the reservoir overburden. Additionally, Mordret et al. (2013) recovered Love waves generated by the operating platform (3 to 29 Hz), and subsequently used those events to produce an S-wave depth profile along a seismic line.

Given that Love waves have displayed higher signal-to-noise ratio than Rayleigh waves at high frequencies (e.g., Lin et al., 2008; Mordret et al., 2013), I build on my previous report (Chang, 2015) and apply the seismic interferometry technique to multicomponent recordings of ambient noise from a small array of ocean-bottom nodes (OBNs) in the North Sea. First, I provide a brief summary of the OBN array and its continuous recordings. Second, I examine the temporal and spatial characteristics of the ambient noise field over a broad frequency range using three methods: spectrograms, plots of spectral energy as a function of distance from the operating platform, and beamforming. Third, I provide an overview of ambient noise cross-correlation with multicomponent data. Finally, I apply the technique to the multiple components of the OBNs at Forties to obtain estimates of inter-station Green's functions over a wide range of frequencies. I am able to recover Scholte waves, Love waves, and an apparent acoustic wave.

CONTINUOUS RECORDINGS FROM FORTIES

The Forties data set, provided to SEP by the Apache Corporation, consists of three groups of OBNs centered at three different platforms in the North Sea. The four-component nodes were deployed as part of an active seismic survey aimed at imaging shallow gas pockets that could pose potential drilling hazards. The nodes were continuously recording, and because active seismic shooting had to be suspended for a couple of days due to rough weather conditions, there is enough ambient noise data to perform seismic interferometry. Furthermore, stormy weather conditions tend to increase the upper limit of the microseism energy (de Ridder and Dellinger, 2011), which is ideal for ambient noise cross-correlations given the limited aperture of each OBN cluster.

For this study, I examine all four components of the Bravo group of OBNs. This cluster of OBNs consists of 52 nodes arranged in a hexagonal shape and centered around an operating platform (Figure 1). The average node spacing is 50 m, and the maximum array offset is approximately 400 m. Each node continuously records for approximately four days at 2 ms sampling and is located roughly 120 m below the sea surface. To prepare the recordings for ambient noise processing, I round the start times up to the nearest quarter of an hour and round down the end times to the nearest quarter of an hour. These times are not the same for all nodes, as they were not all deployed and operating simultaneously.

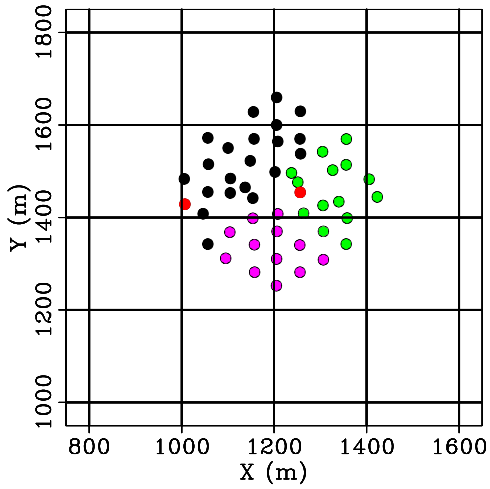

Figure 1: Map of OBNs in the Bravo array. The platform is in the center of the array. Red dots indicate virtual source locations. They are also the nodes that were used to compute spectrograms. The magenta nodes to the south and the green nodes to the east are used for beamforming analysis. [**ER**]

AMBIENT NOISE CHARACTERIZATION

In theory, noise sources must be evenly distributed around the receivers, excite all wave modes with equal energy, and be uncorrelated to accurately estimate Green's functions from ambient noise (Lobkis and Weaver, 2001; Wapenaar, 2004). As these conditions are rarely met in practice, an understanding of the ambient noise field is required for interpreting field data results of the ambient noise cross-correlation method. Here, I characterize the ambient noise field in three ways: spectrograms, spectral energy as a function of offset from the operating platform, and beamforming.

Spectrograms

The spectrograms for the hydrophone and vertical component geophones in Chang (2015) showed that microseism energy (< 1 Hz) was fairly consistent in strength across all nodes, and that platform energy had a strong influence at frequencies between 4 and 8 Hz. Here, I examine the same spectrograms for the full frequency range (up to 250 Hz). I use the same procedure as outlined by Chang (2015).

In all spectrograms, the times of active seismic shooting are clear (short periods around days 109.5 and 110, and from days 111.7-112.5). On the hydrophone components, we see slightly more seismic energy below 40 Hz when the node is near the platform (Figure 2(b)) than when the node is far away from the platform (Figure 2(a)). The same trend is more apparent in the vertical geophones near (Figure 2(d)) and far (Figure 2(c)) from the platform. Because vertical component geophones are typically more sensitive to interface waves than hydrophones (since geophones are coupled to the ground while hydrophones are coupled to the water), it is very likely that the platform is generating interface waves. Above 40 Hz, the seismic energy is roughly the same across corresponding node components, suggesting that the influence of the platform is greatly diminished at these frequencies. It is interesting to note that the trends in seismic energy are not the same across quiet periods (times of no active

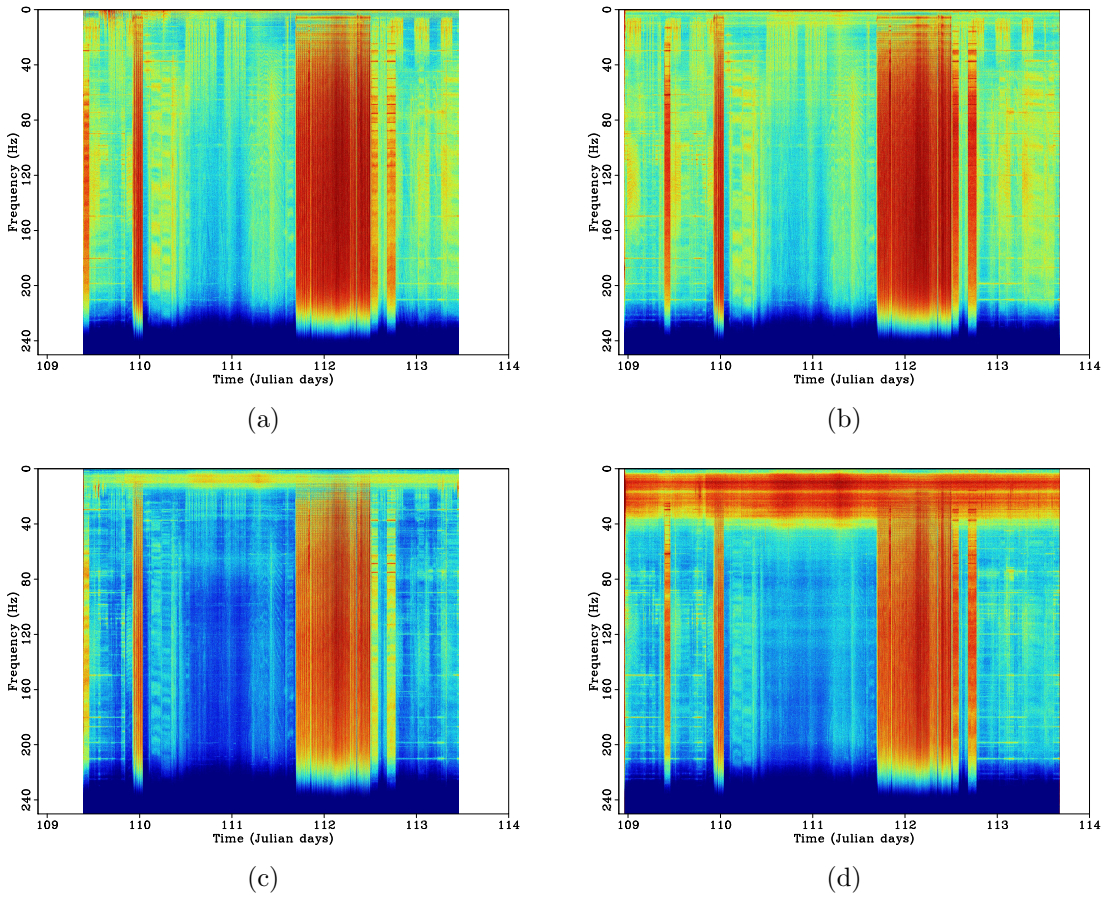

Figure 2: Full-frequency spectrograms computed at two nodes (indicated by red dots in Figure 1). Hydrophone component for (a) western node and (b) eastern node. Vertical component for (c) western node and (d) eastern node. The western node is to the west of the operating platform in the center of the array. Warmer colors indicate higher power. Colors in all plots are clipped the same and are shown in log scale. [**ER**]

seismic shooting). In particular, the quiet period between days 110.4 and 111.3 show relatively high energy up to 80 Hz before tapering off as frequencies increase. This is a different trend than most of the other quiet periods, which display consistent seismic energy across the full frequency range. The presence of seismic energy at high frequencies during supposed quiet periods could be due to distant active seismic shooting at other arrays. Overall, these spectrograms suggest that the influence of the platform extends up to at least 40 Hz, particularly in the vertical geophones. Above 40 Hz, seismic energy is more homogeneously distributed in space.

Platform influence

To gain a better sense of the influence of the platform over all nodes, I plot average spectral power as a function of node distance from the platform over a number of frequency ranges. Spectra are calculated from 30 minutes of recordings starting at Julian day 110.167. Looking from 1.5-2.0 Hz and 5-10 Hz (Figure 3; first and second columns, respectively), we see that average power tapers off as a function of distance from the platform. This supports our belief that the differences in signal power in the spectrograms are caused by the platform. When looking at frequencies between 20 and 40 Hz, the influence of the platform begins to differ depending on the node component. In the hydrophone (Figure 3(c)) the influence of the platform is not very apparent, while in the vertical geophone (Figure 3(g)) the influence of the platform is still clear. Again, both results support the observations from the spectrograms and suggest that the platform has more influence on the vertical geophone than the hydrophone. For frequencies between 40 and 100 Hz, both components show little influence from the platform, suggesting that there is no strong, localized source at such high frequencies. Overall, these results show that the differences in power in the spectrograms can be attributed entirely to the platform.

Beamforming

To determine whether there is any coherent platform energy traveling across the array, I perform plane-wave beamforming (Rost and Thomas, 2002) on 30 minutes of ambient noise recorded by the full array and two subarrays: one south of the platform and one east of the platform (Figure 1). Beamforming of longer recordings did not produce significantly different results. The locations of high amplitudes in the beamforming output reveal the direction from which coherent energy is propagating and at which horizontal slowness it is traveling. Energy along the edges of the plots are spatial aliasing artifacts. Here, I show only the hydrophone results, as the vertical geophone results are very similar.

Beamforming of ambient noise at 1.5-2.0 Hz recorded by the full array (Figure 4(a)) reveals a centered ring of energy and an impulse at zero slowness. The former observation suggests that energy arrives at the array from all directions at

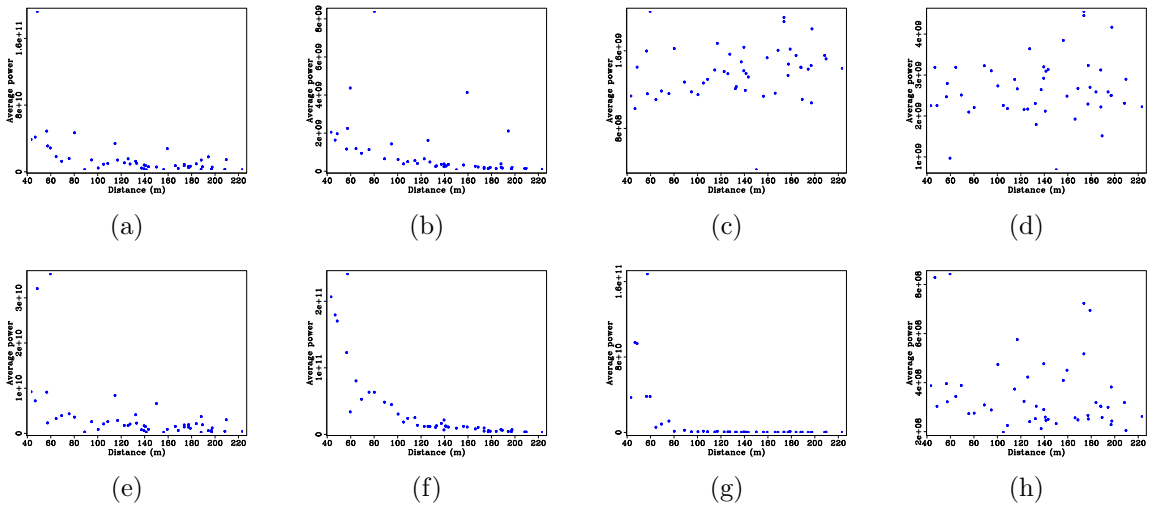

Figure 3: Average spectral power in the hydrophone component (top row) and vertical geophone (bottom row) as a function of distance from the operating platform. First column: 1.5-2.0 Hz. Second column: 5-10 Hz. Third column: 20-40 Hz. Fourth column: 40-100 Hz. [**CR**]

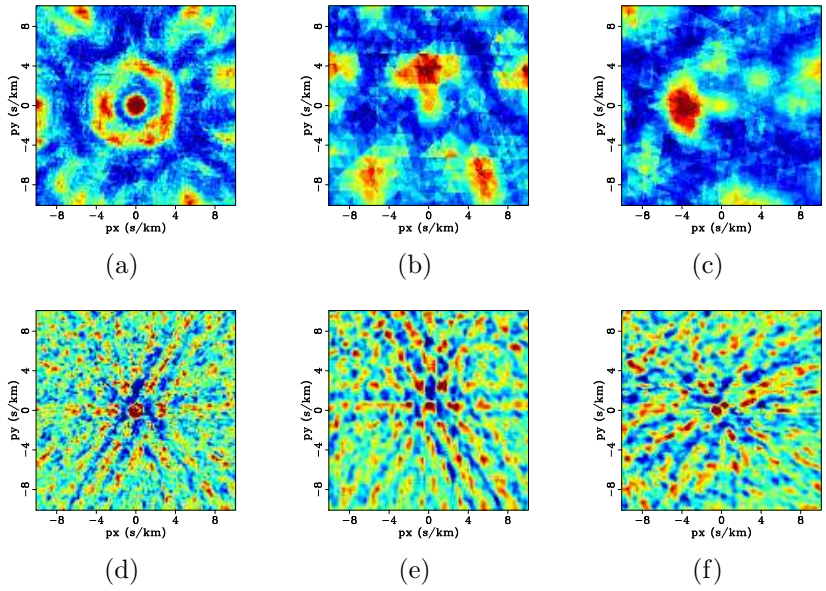

Figure 4: Beamforming results for ambient noise recorded on the hydrophone component. Top row: 1.5-2.0 Hz. Bottom row: 5-10 Hz. Left column: using recordings from all nodes. Middle column: using recordings from southern subset of nodes. Right column: using recordings from eastern subset of nodes. Warmer colors correspond to higher beam power. Color in each panel is clipped independently to enhance features. [**CR**]

approximately 250 m/s, while the latter observation suggests that there is energy reaching all nodes at the same time. However, both these trends disappear when performing beamforming on the two subarrays. Instead, coherent ambient noise at subarrays south (Figure 4(b)) and east (Figure 4(c)) of the platform appear to arrive from the general location of the platform. These events are likely to be platform-generated interface waves traveling at 250 m/s. Because beamforming assumes that the sources of energy are outside the array, the results when using the full array are deceiving due to the presence of the platform in the center of the array. Thus, at this frequency range, it appears that energy is dominated by platform-induced interface waves.

Since we see the influence of the platform at low frequencies, I attempt to find coherent energy emanating from the platform at higher frequencies. Beamforming of ambient noise at 5-10 Hz over the full array (Figure 4(d)) reveals a sharp impulse at zero slowness. Because the platform is in the middle of the array, we cannot trust the features seen in this result. However, when looking at the subarrays to the south (Figure 4(e)) and east (Figure 4(f)) of the platform, we observe similar patterns of streaks. Since the orientation of these streaks are aligned roughly with the orientation of the nodes, we are likely seeing artifacts related to the acquisition geometry. Regardless, there appears to be very little coherent energy at these high frequencies. Overall, the analysis of the ambient noise field at Forties suggests that nearly all the energy from 2-40 Hz in the hydrophone and vertical geophone components emanates from the operating platform.

MULTICOMPONENT SEISMIC INTERFEROMETRY

Understanding that the platform is the main source of noise at frequencies above 2 Hz, I apply the ambient noise cross-correlation technique to all components of the data. For each of the four components (hydrophone; vertical, north, and east geophones), I follow a processing step very similar to the one outlined by Chang (2015). First, I ensure that the recordings are synchronized in time and remove all spurious nodes (leaving 49 of 52 nodes). I then divide the recordings into 30-minute time windows with 50% overlap. This differs from the two-hour time windows used by Chang (2015). I use shorter time windows here because cross-correlating shorter, overlapping records and then summing them leads to more rapid convergence than when cross-correlating longer recordings (Seats et al., 2012). Because there are only about two days of passive data, using smaller windows is particularly advantageous; here I use 209 time windows. Next, I perform ambient noise cross-correlation by calculating the averaged whitened coherency between each pair of nodes for each time window. In the frequency domain, the procedure is generally expressed as:

$$[G(x_B, x_A, \omega) + G^*(x_B, x_A, \omega)] = \left\langle \left(\frac{U(x_B, \omega)}{\{|U(x_B, \omega)|\}} \right) \left(\frac{U^*(x_A, \omega)}{\{|U(x_A, \omega)|\}} \right) \right\rangle, \quad (1)$$

where G is the Green's function between two receiver locations (x_A, x_B), $U(x, \omega)$ is the spectrum of the wavefield at a given receiver location x, $*$ is the complex

conjugate, $\langle\cdot\rangle$ is the time-averaged ensemble, $|\cdot|$ is the magnitude of the spectrum, and $\{\cdot\}$ is a 0.003 Hz running window average used for normalizing the signal. In the case of the horizontal geophone components, this procedure differs slightly in that the north and east components are whitened together instead of individually. In particular, I choose to whiten both components by their average smoothed spectrums. This step maintains the commutativity of any rotation operator, which helps save computational time by delaying the rotations until after correlating the signals.

Chang (2015) attempted to extract Scholte waves generated by the platform in the hydrophone and vertical geophone components. Though there was correlating energy, it was too noisy to interpret at high frequencies. Because other studies have suggested that Love waves can have higher signal-to-noise ratios than Rayleigh (or Scholte) waves (e.g., Lin et al., 2008; Mordret et al., 2013), I examine correlations in the transverse (T) and radial (R) components for each node in hopes of extracting clear seismic events generated by the platform. To obtain correlations in these components for a single node, I transform them from the east (E) and north (N) component correlations using:

$$\begin{bmatrix} TT \\ RR \end{bmatrix} = \begin{bmatrix} -\cos(\theta)\cos(\phi) & \cos(\theta)\sin(\phi) & -\sin(\theta)\sin(\phi) & \sin(\theta)\cos(\phi) \\ -\sin(\theta)\sin(\phi) & -\sin(\theta)\cos(\phi) & -\cos(\theta)\cos(\phi) & -\cos(\theta)\sin(\phi) \end{bmatrix} \begin{bmatrix} EE \\ EN \\ NN \\ NE \end{bmatrix}, \quad (2)$$

where θ is the inter-station azimuth and ϕ is the corresponding back-azimuth (Lin et al., 2008). These angles are defined by setting the first station as the source location and the second station as the receiver location. After this rotation, I expect to observe Love waves in the transverse component and Scholte waves in the radial component.

Correlating one node with all other nodes creates a virtual source gather. I first examine correlations between the two nodes near and far from the platform (red dots in Figure 1) and all nodes between 1350 and 1500 m in the north-south direction. Gathers are sorted by virtual source-receiver offset in the east-west direction. Looking at correlations in the microseism band (0.5-1.0 Hz), we see coherent events in all gathers and components (Figure 5). Given that interface waves typically dominate the energy in the microseism band, we are likely seeing Love waves in the transverse component (Figure 5; top row) and Scholte waves in the radial component (Figure 5; bottom row). Though Chang (2015) mentioned that offsets at Forties were too short to reliably pick travel times of these events, these coherent correlations at least suggest that the rotation into the transverse and radial components is reasonable. In correlations from 5-10 Hz, we see noisy but coherent patterns (Figure 6) that are indicative of localized noise sources. Looking at the gather where the virtual source is to the west of the platform (Figure 6; left column), most of the energy is at acausal times, with a corner point around receiver index 14. In these plots, the zero-offset trace is receiver index 2. The corner point corresponds to the approximate offset of the plat-

form from the virtual source location. When the virtual source and the receiver are on the same side of the platform, the corresponding acausal energy represents energy traveling from the platform toward the virtual source. The similar moveout pattern for correlations between nodes on opposite sides of the platform is characteristic of active noise sources. Looking at the gather where the virtual source is at the platform (Figure 6; right column), we see that there is clear moveout from the virtual source location (receiver index 16) at only causal times. Since causal energy corresponds to energy traveling outward from the virtual source location, this pattern supports the belief that the correlations at these frequencies are dominated by energy generated by the platform. Given travel times of approximately 2 s over a distance of 200 m (the distance between the farthest node and the platform), I estimate these events to be traveling at approximately 100 m/s. Thus, the energy from the platform is likely appearing in the correlations as interface waves (Love waves in the transverse component and Scholte waves in the radial component).

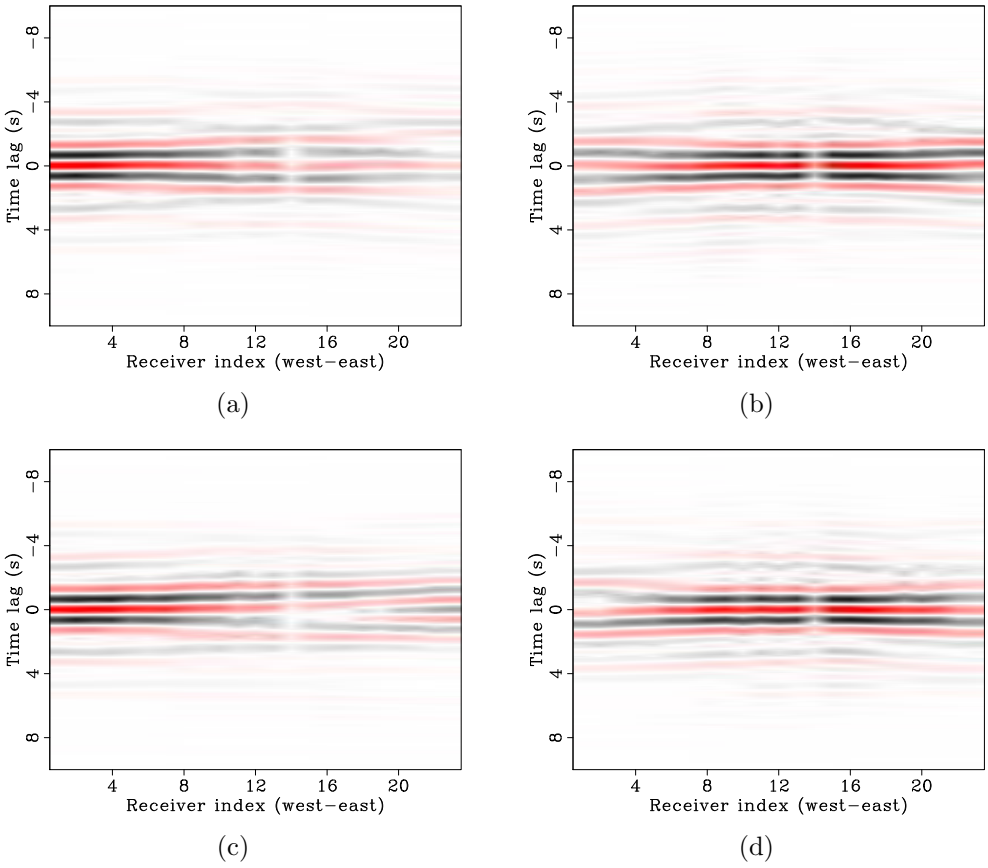

Figure 5: Virtual source gathers in the microseism band (0.5-1.0 Hz). Top row: transverse-transverse correlations. Bottom row: radial-radial correlations. Left column: node west of platform (zero-offset trace is receiver index 2). Right column: node near platform (zero-offset trace is receiver index 16). [**CR**]

Because I have a small array that may be able to capture very high-frequency events, I examine correlation results from hydrophones and vertical geophones for

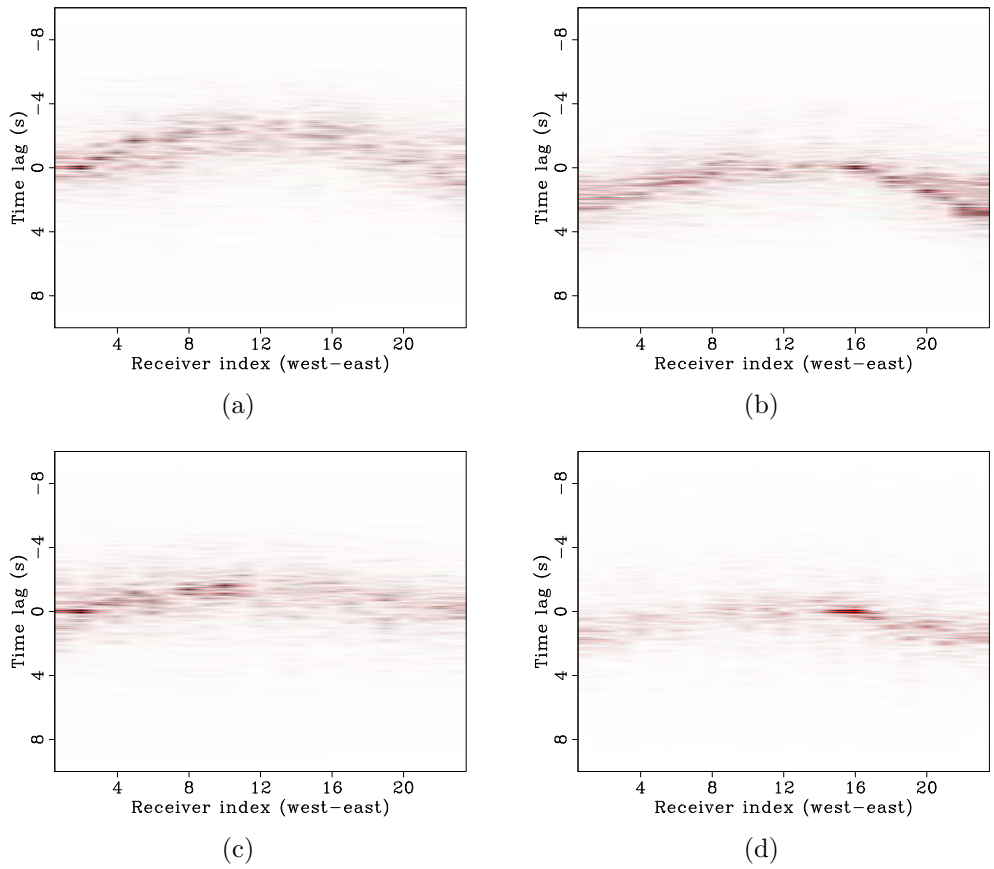

Figure 6: Virtual source gathers from 5-10 Hz. Top row: transverse-transverse correlations. Bottom row: radial-radial correlations. Left column: node west of platform (zero-offset trace is receiver index 2). Right column: node near platform (zero-offset trace is receiver index 16). The moveout velocities of these events are approximately 100 m/s. [**CR**]

frequencies between 40 and 80 Hz. Unlike with the previous virtual source gathers, I plot correlations as a function of absolute offset between the virtual source and receiver to make it easier to identify any event. From hydrophone component correlations (Figure 7; top row), we are able to see a noisy event with a moveout of approximately 1350 m/s (given an estimated arrival time of 0.3 s at a receiver 400 m away for the western virtual source and an estimated arrival time of 0.15 s at a receiver 200 m away for the eastern virtual source). This event also appears in the vertical geophone correlations (Figure 7; bottom row), although it is even noisier than the hydrophone correlations. This event has a velocity close to that of water and is stronger in the hydrophone component, which suggests that this event is an acoustic wave. Given that most of the energy is at acausal times when the virtual source is west of the platform (Figure 7; left column), and that most of the energy is at causal times when the virtual source is at the platform (Figure 7; right column), it is likely that this apparent acoustic wave is also generated by the platform.

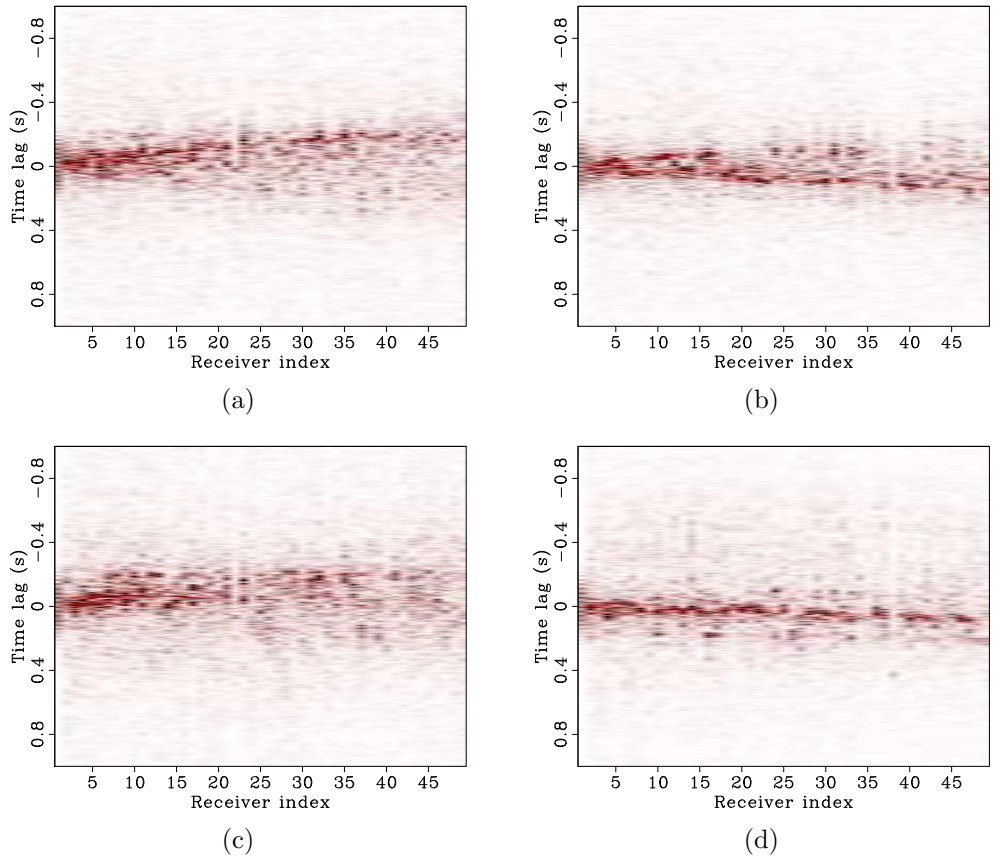

Figure 7: Correlations showing an apparent acoustic wave at frequencies 40-80 Hz. Top row: Hydrophone-hydrophone correlations. Bottom row: Vertical-vertical geophone correlations. Left column: node west of platform. Right column: node near platform. The moveout velocities of these events are approximately 1350 m/s. Note the change in the time range compared to the previous virtual source gathers. [**CR**]

DISCUSSION

In all my analyses, it is clear that the platform dominates the ambient noise field. The ambient noise analyses suggest that the influence of the platform goes up to 40 Hz, and my ambient noise cross-correlations suggest that the platform is generating coherent seismic signals up to 80 Hz. However, though we observe coherent interface waves in the radial and transverse components, these noisy events need further analysis to verify their reliability. While Love waves typically travel faster than Scholte waves at a given frequency, it appears that they are traveling slightly slower in these gathers. However, given the noisy signal and limited maximum offset, estimating velocity directly from these gathers is unreliable. It does appear, though, that the Love-wave event has a higher signal-to-noise ratio than the Scholte-wave event. This observation is consistent with results from Lin et al. (2008) and Mordret et al. (2013). Overall, it is promising that there is apparent interface-wave energy at such high frequencies. Given the limited aperture of the array, high-frequency interface waves (and the associated short wavelengths) will be needed to perform any sort of tomography procedure.

Additionally, it is potentially promising that there are signs of an acoustic wave in the correlations for passive fathometry. Briefly, passive fathometry relies on down-going acoustic waves generated by the sea surface and their reflections to obtain a shallow reflection profile (Gerstoft et al., 2008; Siderius et al., 2010). Essentially, the process involves a cross-correlation of up- and down-going passive energy. The presence of a passively-generated acoustic wave (likely generated by the platform) is encouraging for any search for vertically-propagating acoustic waves. Perhaps such an event could be generated by waves breaking strongly against the platform. Note that the acoustic wave in my correlations is likely close to horizontally propagating, though, given that the approximate velocity is slightly less than water velocity. This sort of event would be noise in passive fathometry. Regardless, it is promising that there appears to be passively-generated acoustic waves at Forties.

CONCLUSIONS

The location and geometry of the Apache Forties OBN survey allows for the application of the high-frequency, multicomponent ambient noise cross-correlation technique. Spectrograms and plots of spectral power as a function of distance from the platform suggest that the operating platform dominates the ambient noise field for frequencies up to 40 Hz. Additionally, the influence of the platform at these frequencies is stronger in the vertical geophone than the hydrophone, which indicates that the platform is primarily generating interface waves. Beamforming of the ambient noise field recorded by subarrays also indicate the strong influence of the platform. From correlations in the transverse and radial components, we see indications of Love waves and Scholte waves, respectively, between 2 and 10 Hz. Though they are noisy, particularly at high frequencies, they are clearly generated by the platform and are potentially useable in a tomography procedure. From 40-80 Hz, there are apparent acoustic waves in the

hydrophone and vertical geophone components. The presence of passively-produced acoustic waves is promising for passive fathometry.

ACKNOWLEDGMENTS

The author would like to thank Apache North Sea Limited for access to the data set and permission to publish. The author also thanks Biondo Biondi, Shuki Ronen, and Stewart Levin for help processing the data and useful discussions. Finally, the author would like to thank the sponsors of the Stanford Exploration Project for their financial support.

REFERENCES

Bensen, G., M. Ritzwoller, and N. Shapiro, 2008, Broadband ambient noise surface wave tomography across the United States: Journal of Geophysical Research: Solid Earth, **113**.

Chang, J. P., 2015, Processing of continuous data at Apache Forties for seismic interferometry: SEP-Report, **160**.

Chang, J. P., S. A. de Ridder, and B. L. Biondi, 2016, High-frequency Rayleigh-wave tomography using traffic noise from Long Beach, California: Geophysics, **81**, B1–B11.

de Ridder, S. and J. Dellinger, 2011, Ambient seismic noise eikonal tomography for near-surface imaging at Valhall: The Leading Edge, **30**, 506–512.

Gerstoft, P., W. S. Hodgkiss, M. Siderius, C.-F. Huang, and C. H. Harrison, 2008, Passive fathometer processing: The Journal of the Acoustical Society of America, **123**, 1297.

Lin, F.-C., D. Li, R. Clayton, and D. Hollis, 2012, Interferometry with a dense 3D dataset: SEG Technical Program Expanded Abstracts, **1**, 1–6.

Lin, F.-C., M. P. Moschetti, and M. H. Ritzwoller, 2008, Surface wave tomography of the western United States from ambient seismic noise: Rayleigh and Love wave phase velocity maps: Geophysical Journal International, **173**, 281–298.

Lobkis, O. I. and R. L. Weaver, 2001, On the emergence of the Green's function in the correlations of a diffuse field: The Journal of the Acoustical Society of America, **110**, 3011–3017.

Mordret, A., M. Landès, N. Shapiro, S. Singh, P. Roux, and O. Barkved, 2013, Near-surface study at the valhall oil field from ambient noise surface wave tomography: Geophysical Journal International, ggt061.

Rost, S. and C. Thomas, 2002, Array seismology: methods and applications: Reviews of Geophysics, **40**, 2–1.

Seats, K. J., J. F. Lawrence, and G. A. Prieto, 2012, Improved ambient noise correlation functions using Welch's method: Geophysical Journal International, **188**, 513–523.

Shapiro, N. M., M. Campillo, L. Stehly, and M. H. Ritzwoller, 2005, High-resolution surface-wave tomography from ambient seismic noise: Science, **307**, 1615–1618.

Siderius, M., H. Song, P. Gerstoft, W. S. Hodgkiss, P. Hursky, and C. Harrison, 2010, Adaptive passive fathometer processing: The Journal of the Acoustical Society of America, **127**, 2193.

Snieder, R., 2004, Extracting the Green's function from the correlation of coda waves: A derivation based on stationary phase: Physical Review E, **69**, 046610.

Wapenaar, K., 2004, Retrieving the elastodynamic Green's function of an arbitrary inhomogeneous medium by cross correlation: Physical Review Letters, **93**, 254301.

Yang, Y., M. H. Ritzwoller, F.-C. Lin, M. Moschetti, and N. M. Shapiro, 2008, Structure of the crust and uppermost mantle beneath the western United States revealed by ambient noise and earthquake tomography: Journal of Geophysical Research: Solid Earth, **113**.